Journal of Alloys and Compounds 855 (2021) 157438

Contents lists available at ScienceDirect

Journal of Alloys and Compounds

journal homepage: http://www.elsevier.com/locate/jalcom

Morphology-control and template-free fabrication of bimetallic Cu–Ni alloy rods for ethanol electro-oxidation in alkaline media

Zelin Miao [a, 1], Changfan Xu [a, 1], Jing Zhan [a, b, *], Ziwei Xu [a]

[a] School of Metallurgy and Environment, Central South University, Changsha, 410083, China
[b] National Engineering Laboratory for High Efficiency Recovery of Refractory Nonferrous Metals Resources, Changsha, 410083, China

ARTICLE INFO

Article history:
Received 15 June 2020
Received in revised form
25 September 2020
Accepted 1 October 2020
Available online 6 October 2020

Keywords:
Coordination-coprecipitation
Cu–Ni alloy rods
Porous nanostructure
Ethanol electro-oxidation

ABSTRACT

The design of highly efficient and stable non-noble transition metal-based electrocatalysts for the ethanol oxidation reaction (EOR) is imperative for the development of the direct ethanol fuel cells (DEFCs). In this work, we report a simple template-free method for preparing a type of rod-like Cu–Ni alloy particle with the unique porous structure and evaluate it as the electrocatalyst for the EOR in alkaline media. The pH, which was adjusted by the addition of $NH_3 \cdot H_2O$ during the liquid-phase coprecipitation process, was found to be a key factor to shape Cu–Ni alloy precursor into a quasi-one-dimensional morphology. After annealing at a reducing atmosphere (H_2/Ar = 5/95, v/v), well-alloyed Cu–Ni rods with the predefined molar ratio (Cu/Ni) of 1:1, a specific surface area of 6.84 $m^2\ g^{-1}$, and the average pore size of 30.97 nm were obtained. Cyclic voltammetry (CV) and chronoamperometry (CA) test results show that the prepared Cu–Ni alloy catalyst demonstrated an anodic current peak of 86.10 mA cm^{-2} in the presence of 0.2 M ethanol and a 95% retention of current density after 2000 s, indicating its good electrochemical performance in terms of catalytical activity and long-term stability. This bottom-up synthesis strategy would enrich the fabrication methodologies and open up a promising avenue for preparing multiple Ni-based EOR electrocatalysts with the easy-controllable morphologies and porous structure at the industrial scale.

1. Introduction

Due to the large consumption of fossil fuels and environmental pollution, direct ethanol fuel cells (DEFCs), an environmentally-benign and highly-efficient energy conversion device, have drawn increasing attention with the great potentials to be applied in portable electronics and electrical vehicles [1–3]. However, the sluggish kinetics of ethanol oxidation reaction (EOR) has always been regarded as a critical issue in DEFCs, which needs to be circumvented by the utilization of high-performance electrocatalysts [4,5]. While many pieces of researches focused on Pt/Pd and their alloys or composites [4–8], the deficient global reserves of noble metals and their vulnerability to CO poisoning have severely restricted industrial-scale manufacturing and commercial utilities of these materials [9–11].

Cu–Ni alloy, as one of the Ni-based electrocatalysts, exhibits several advantages including good surface oxidation properties, excellent electrical conductivity, and superior corrosion tolerance in alkaline media [12,13], making it a popular choice for numerous energy conversion processes such as methane decomposition [14], hydrogen evolution reaction (HER) [15,16], and oxidation reaction of small organic molecules (SOMs) [17–19]. When catalyzing electro-oxidation of methanol, Cu–Ni alloy was found to exhibit a low affinity of CO, which significantly ameliorates the self-poisoning issue facing by the noble-metal-based materials [18]. Moreover, the addition of the Cu component could properly modify the electronic structure of Ni and suppress the formation of destructive intermediate γ-NiOOH during the electrocatalytic process, leading to improved activity and stability for electro-oxidation of SOMs [17]. For example, Habibi et al. [19] fabricated dendritic-morphology Cu–Ni alloy nanoparticles via an electro-deposition approach, which showed higher anodic current density compared with pure Ni towards the oxidation of glycerol.

Apart from the manipulation of elemental composition, the performance of electrocatalysts can be further improved by

* Corresponding author. School of Metallurgy and Environment, Central South University, Changsha, 410083, China..
E-mail address: zhanjing@csu.edu.cn (J. Zhan).
[1] The authors have equal contributions.

https://doi.org/10.1016/j.jallcom.2020.157438
0925-8388/

optimizing the morphology and structure, i.e., to help expose an increased density of active sites on the surface of the corresponding materials [4,20]. Resulting from Ostwald ripening and potential coalescence of particles through migration [21,22], zero-dimensional (0D) materials/nanoparticles with high surface energy usually present poor stability, which can be alleviated by endowing the electrocatalysts with one-dimensional (1D) morphology. Meanwhile, the simultaneously increased electrical conductivity originated from the interconnection of the anisotropic conductor could facilitate electron transportation and further eliminate the usage of carbon supports [20,23]. Furthermore, the addition of the porous nanostructure with the increased specific surface area (SSA) is expected to promote the mass transfer such as diffusion of ions at the interface of electrode and electrolyte [10,24,25]. Although many fabrication methods for Cu–Ni alloy have currently been reported such as mechanical alloying [26], electrodeposition [27], laser ablation [28], spray pyrolysis [29], etc., most of them failed to prepare Cu–Ni alloy with the aforementioned 1D morphology and porous structure. Template-based methods may achieve this goal by applying easy-etched templates, e.g., anodic alumina membranes (AAMs), to precisely control the morphology and particle size distribution [30]. However, one should notice that the preparation of the ordered AAMs was a two-step anodizing process, which would undoubtedly impose complexity and increased cost to the whole fabrication procedure. Thus, the exploration of new methods for the fabrication of 1D porous Cu–Ni alloy with low cost, mild temperature, and facile control over the morphology and particle size is still indispensable.

Herein, we reported a simple template-free strategy for preparing 1D porous Cu–Ni alloy particles by combining coprecipitation of metal ions (i.e., Cu^{2+} and Ni^{2+}) into Cu–Ni alloy precursors from Cu^{2+}-Ni^{2+}-NH_3-NH_4^+-$C_2O_4^{2-}$-Cl^--H_2O system, with an annealing process. However, in this reaction system, four orders of magnitude difference of cumulative formation constants of Cu/Ni complexes with NH_3 ligand indicates their thermodynamically unfavorable simultaneous precipitation from the liquid phase at the high pH [31], leading to the hard control over elemental distribution and metallic ratio in Cu–Ni alloy precursors and the corresponding alloy products. In this work, this issue was solved by applying the ethanol-H_2O mixture as the modified solvent instead of pure H_2O, and the efficacy of pH on the morphology of precursors was systematically investigated. Further, the NH_3-induced oriented growth mechanism for rod-like Cu–Ni oxalate complex salt was proposed. Following thermal decomposition in a reducing atmosphere, bimetallic Cu–Ni rods with the predefined molar ratio (Cu/Ni) of 1:1 and a hierarchically porous structure were obtained. Their application as electrocatalysts for the EOR in NaOH solution was subsequently evaluated by cyclic voltammetry (CV) and chronoamperometry (CA) techniques.

2. Experimental

2.1. Materials preparation

All chemical reagents were of analytical grade and used without further purification. In a typical process, $H_2C_2O_4 \cdot 2H_2O$ (13.010 g, 0.100 mol) and polyvinylpyrrolidone (PVP, 0.500 g) were dissolved in a solvent mixture comprising 50 mL ethanol (EtOH) and 50 mL deionized (DI) water. To this was injected a solution of $NiCl_2 \cdot 6H_2O$ (9.702 g, 0.040 mol), 7.842 g of $CuCl_2 \cdot 2H_2O$ (7.842 g, 0.046 mol) and PVP (0.500 g) in 50 mL ethanol and 50 mL DI water, at the constant rate of 1.67 mL min^{-1} in 60 min. The reaction mixture was mechanically stirred in a water bath maintained at 323 K, during which the pH was carefully adjusted to 2.0–8.0 by dropwise addition of $NH_3 \cdot H_2O$. After completion of feeding, the suspension was stirred for an additional 2 h. Precipitated solids were then filtered, rinsed several times with DI water and ethanol, and dried in a vacuum oven at 353 K for 12 h. Finally, the precursors were decomposed in a reducing atmosphere (H_2/Ar = 5/95, v/v) at 673 K for 30 min to obtain the porous bimetallic Cu–Ni rods. Ni powders with a similar quasi-1D porous fashion were also prepared and the corresponding physical characterizations were reported in our previous work [32,33].

2.2. Materials characterizations

The morphology and elemental ratio/distribution of the samples were systematically investigated by transmission electron microscopy (TEM, Tecnai G2 20ST), scanning electron microscopy (SEM, JSM-6360LV), and the affiliated energy-dispersive X-ray spectroscopy (EDX, GENESIS 60S). The powder XRD patterns of the precursors and final products were recorded by an X-ray diffractometer (Rigaku-TTRIII X, Cu, λ = 0.154056 nm) with the scanning rate of 10° min^{-1}. Characterization of the chemical composition of Cu–Ni alloy precursors was achieved by Fourier transform infrared spectrometry (FTIR, Nicolet 6700) in the wavenumbers ranging from 400 to 4000 cm^{-1}. The thermal decomposition profile of the rod-like Cu–Ni alloy precursor (obtained at pH = 7.6) was recorded by thermogravimetry and differential thermal analyses (TA, SDTQ). X-ray photoelectron spectroscopy (XPS, Thermo Scientific K-Alpha) with Al K_α as the excitation source was utilized to probe the surface chemical composition and valence states. The Brunauer-Emmett-Teller (BET) surface area and the distribution of pore size were measured by the surface area and porosity analyzer (Micromeritics ASAP 2020).

2.3. Electrochemical measurements

The electrocatalyst ink was prepared by ultrasonic dispersion of 25 mg of Cu–Ni alloy powders in 1 mL DI water. Then, 4 μL of this suspension was deposited onto the surface of the glassy carbon electrode (GCE, diameter: 3 mm) that had been mechanically polished by 50 nm γ-Al_2O_3 slurry and rinsed with DI water and ethanol for several times. Nafion solution (5 wt%, 2 μL) was added on the top of the dried electrocatalyst ink to obtain the modified electrode (Cu–Ni/GCE). Ni/GCE was also prepared using the same drop-casting method. All electrochemical measurements were performed at room temperature (298 ± 2 K) with an electrochemical workstation (CHI660B) using a conventional three-electrode setup. The modified glass carbon electrode (Cu–Ni/GCE and Ni/GCE) with a mass loading of 1.41 mg cm^{-2}, a saturated calomel electrode (SCE), and a Pt electrode (1 cm × 1 cm) served as working, reference, and counter electrode, respectively.

3. Results and discussions

3.1. Shape-controlled synthesis of Cu–Ni alloy precursors

The Cu–Ni alloy rods were synthesized through a coordination-coprecipitation procedure coupled with the thermal decomposition in a reducing atmosphere as illustrated in Fig. 1, where the liquid-phase precipitation process has a significant influence on morphology, composition homogeneity, and elemental distribution of the final Cu–Ni alloy particles. According to the previous thermodynamic analysis of the Ni–Co system [34], the simultaneous precipitation of Cu^{2+} and Ni^{2+} by $C_2O_4^{2-}$ with the assistance of NH_3 in Cu^{2+}-Ni^{2+}-NH_3-NH_4^+-$C_2O_4^{2-}$-Cl^--H_2O (298 K) system would also be a complicated dynamic equilibrium process, during which many reactions coexist and compete with each other. These include the coordination of Cu^{2+}/Ni^{2+} with NH_3 and $C_2O_4^{2-}$, hydrolysis of metal

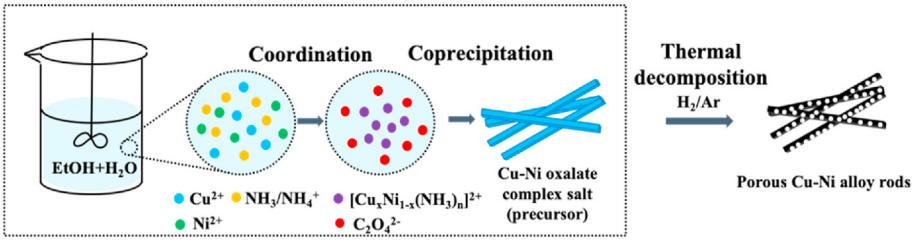

Fig. 1. Schematic illustration of the fabrication process for rod-like porous Cu–Ni alloy.

ions, precipitation of Cu^{2+}/Ni^{2+} by $C_2O_4^{2-}$, and dissociation reactions of weak acids and bases [35]. To determine the theoretical pH ranges for coprecipitation of Cu^{2+} and Ni^{2+} in the water solvent, a thermodynamic analysis was performed according to the principle of matter conservation [34–36] and the calculation process will be illustrated in another work in detail. It is concluded that due to the lower dissociation constants of $[Cu(NH_3)_n]^{2+}$(n = 1–5) [35] compared with $[Ni(NH_3)_m]^{2+}$(m = 1–6) [34], the total concentration of Cu^{2+} (free ions and complexes) in solution is higher than Ni^{2+} at most time, except for pH ranging from 2 to 6. This makes it difficult to keep the molar ratio (1:1, for example) of metallic components in precursors prepared at a higher pH and the corresponding alloy products the same to the ratio of the initial concentration of the metal ions added into the system. To expand the coprecipitation pH range of Cu^{2+} and Ni^{2+}, the ethanol-water mixture was employed as the reaction solvent to replace pure water since the addition of a low dielectric medium, such as ethanol, was found to have an obvious effect to adjust the thermodynamics of precipitation reaction [37] and to decrease the solubility of oxalate salts and metal-NH_3 complexes [34]. Moreover, ethanol has lower surface tension compared with water, which is conducive to reducing the particle size and improving the quality and dispersion degree of Cu–Ni alloy precursors [38]. These could also be assisted by adding the proper quantity of PVP, which serves as the surface stabilizer and dispersion reagent during the nucleation and crystal growth process [39,40]. After the annealing treatment, Cu–Ni alloy rods with the even distribution of Cu and Ni, an accurate molar ratio of 1:1, and a unique porous nanostructure can be finally obtained.

The SEM images of Cu–Ni alloy precursors obtained at different pH are shown in Fig. 2. It can be observed that the solution pH, which was initially acidic due to the existence of $H_2C_2O_4$ and then adjusted by $NH_3\cdot H_2O$, has a prominent effect on the morphology and particle size of the precursors. At pH = 2.0 (Fig. 2a), these form as irregular particles intertwined by numerous tiny fibers. At pH = 5.0 (Fig. 2b), the morphology changes to micro-spheres agglomerated by nanoparticles. By increasing the pH to 7.6 (Fig. 2c), distinct rod-like Cu–Ni alloy precursors are observed with an aspect ratio larger than 10. We can conclude that the shape of precursors could be simply controlled by adjusting the addition of $NH_3\cdot H_2O$ as the morphology of precursors experienced from irregular aggregates to micro-spheres, further to rod-like particles. However, when the pH reaches to 8.0, the clusters of rods are likely to be corroded [41], leading to the significant decrease of the uniformity of precursors, as shown in Fig. 2d. Meanwhile, some deep blue crystals were observed after filtration, which are supposed to be copper oxalate particles derived from the segregated precipitation of Cu^{2+} at such high pH value. Therefore, to obtain the uniform rod-like Cu–Ni alloy precursor powders from the modified reaction system of Cu^{2+}-Ni^{2+}-NH_3-NH_4^+-$C_2O_4^{2-}$-Cl^--ethanol-H_2O, the pH of the reaction system should be maintained at 7.6.

Fig. 3 shows the XRD patterns of Cu–Ni alloy precursors obtained at different pH values. Cu–Ni oxalate salts in the absence of $NH_3\cdot H_2O$ were also synthesized and measured for comparison. It can be seen that precursor prepared without $NH_3\cdot H_2O$ (pH = 0.42 during the reaction) has the same diffraction peaks as those prepared at pH = 2.0 and 5.0. Their peaks overlap with those of $CuC_2O_4\cdot xH_2O$ and $NiC_2O_4\cdot 2H_2O$, indicating that these precursors are essentially the mechanical mixture of Cu and Ni oxalate salts. However, when pH = 7.6 and pH = 8.0, the XRD patterns have a significant change which implies the formation of new substances and no existing standard JCPDS cards could be currently referenced for them. We consider that the addition of excess $NH_3\cdot H_2O$ would be the reason for the induction of the rod-like morphology, as the pH of the solution was the only parameter that we changed.

To confirm this hypothesis, the infrared spectra of the corresponding Cu–Ni alloy precursors were further measured as shown in Fig. 4. When pH ≤ 5.0, the infrared spectra are similar. As for the precursor obtained at pH = 2, the absorption peak at 3419.83 cm^{-1} and 1628.76 cm^{-1} can be ascribed to –OH in the water of crystallization [42]. The peaks located at 1358.02 cm^{-1} and 1319 cm^{-1} can be assigned to C–O stretching and O–C=O bending vibrations. Moreover, the stretching vibration of Me–O contributes to the absorption peak at 760 cm^{-1} [43] and the absorption peak located at 489.26 cm^{-1} is resulting from the oxalate ring deformation [32]. Unsurprisingly, several peaks related to NH_3 appear in the spectra of precursor samples obtained at high pH. For example, when pH = 7.6, the original peak located at 3341.83 cm^{-1} splits into two peaks at 3443.64 cm^{-1} and 3351.41 cm^{-1}, corresponding to the stretching vibration of –OH and N–H, respectively. A new absorption peak at 1300 cm^{-1} could be related to the bending vibration of H–N–H and the peak at 691.57 cm^{-1} is generated by the rocking vibration of NH_3 [44]. The appearance of these new peaks confirms the existence of NH_3 in Cu–Ni alloy precursors obtained at pH = 7.6 and 8.0.

According to the above characterizations and analysis, we proposed that under alkaline conditions, e.g., pH = 7.6 and 8.0, NH_3 would coordinate with Cu^{2+}/Ni^{2+} and be transferred into precipitated solids, leading to the significant change of XRD patterns and infrared spectra of Cu–Ni alloy precursors comparing with those obtained at low pH conditions; the chemical formulas of resulting precursors at high pH can be preliminarily inferred to $Cu_xNi_{1-x}(NH_3)_yC_2O_4\cdot nH_2O$ (x: 0–1; y: equivalents of coordinated NH_3; n: equivalents of water of crystallization), where the values of x, y, and n remain to be determined in the further study. The suggested growth mechanism of rod-like Cu–Ni alloy precursor containing NH_3 is accordingly put forward and schematically illustrated in Fig. 5. Similar to copper oxalate previously studied [45], Cu–Ni oxalate complex salts at low pH are constructed by $[M(C_2O_4)]_n$ (M = Cu/Ni) ribbons where the adjacent two ribbons are perpendicular to each other. Each metal center can form bonds with four oxygen atoms donated by two $C_2O_4^{2-}$ ligands in a plane and two oxygen atoms from $C_2O_4^{2-}$ of upper and lower ribbons. With the excessive addition of $NH_3\cdot H_2O$, i.e. under alkaline conditions, NH_3

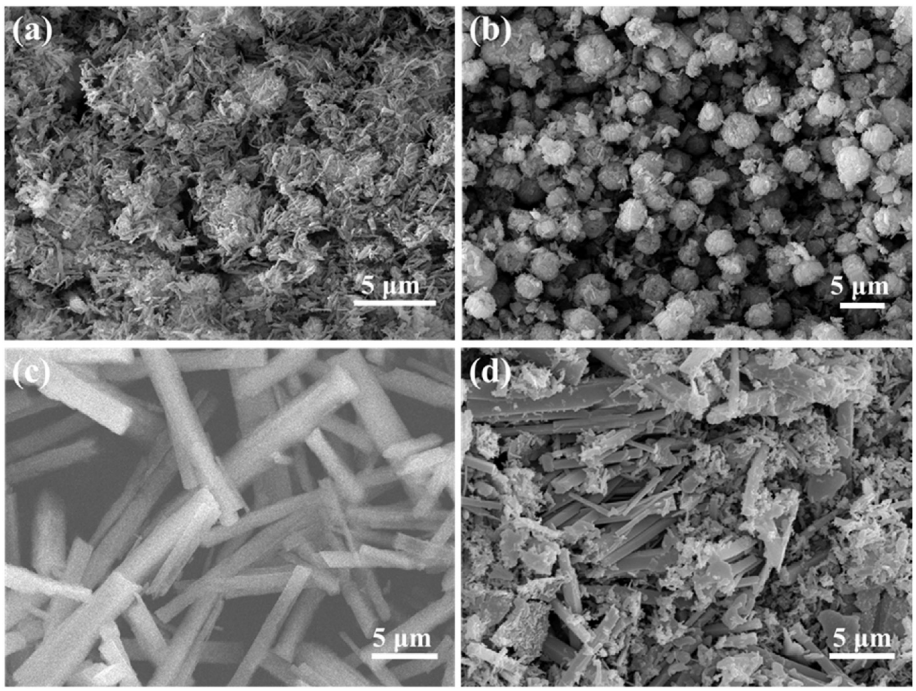

Fig. 2. SEM images of Cu–Ni alloy precursors prepared at different pH conditions: (a) 2.0, (b) 5.0, (c) 7.6, and (d) 8.0.

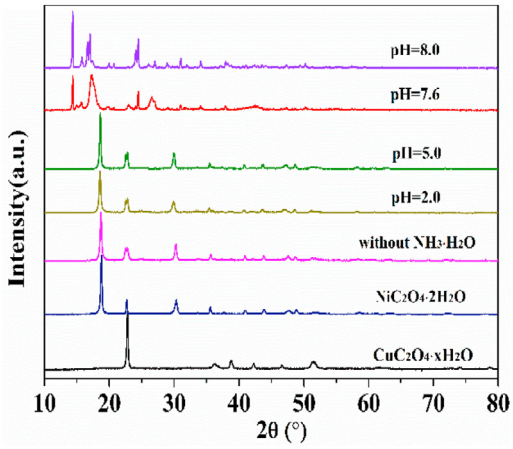

Fig. 3. XRD patterns of Cu–Ni alloy precursors prepared at different pH conditions.

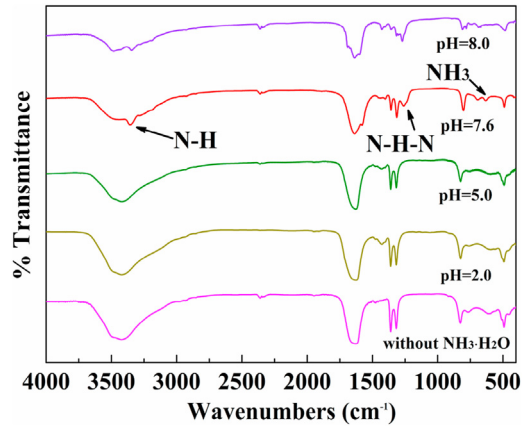

Fig. 4. Infrared spectra of Cu–Ni alloy precursors prepared at different pH conditions.

molecules are preferentially coordinated with metal centers, leading to the change of the original surface polarity and further surface energy of Cu–Ni oxalate crystal [41,45]. Through the ordered aggregation of crystallites in a certain direction under the action of surface energy disparity [46], the Cu–Ni oxalate complex salts with a quasi-one-dimensional morphology are finally fabricated. While at low pH (pH = 5.0), the precursors display as micro-spheres aggregated by numerous nanocrystals.

3.2. Preparation of porous Cu–Ni alloy rods

The thermal decomposition behaviors of rod-like Cu–Ni alloy precursors obtained at pH = 7.6 were investigated by the thermogravimetric analyzer and the corresponding TG-DTA curves were recorded as depicted in Fig. 6a. A continuous mass loss was observed as the temperature increased up to 370 °C. Four endothermic peaks at 190.35 °C (weight loss: 6.86%), 231.73 °C (weight loss: 22.46%), 311.43 °C, and 349.37 °C (weight loss:35.86%) could be assigned to the primary and secondary removal of water of crystallization, volatilization of coordinated NH_3 and decomposition of residual Cu–Ni complex oxalate salt, respectively. It should be noted that the thermal decomposition temperature of CuC_2O_4 and NiC_2O_4 in an Ar atmosphere was reported to be 295 °C [47] and 370 °C [32]. Therefore, the single endothermic peak at 349.37 °C displayed in Fig. 6a represents that the as-prepared Cu–Ni alloy precursor is a type of novel compound rather than a simple mixture of NH_3-coordinated CuC_2O_4 and NiC_2O_4 powders. Fig. 6b shows the XRD pattern of the decomposed sample from rod-like precursor at 673 K in a weak reducing atmosphere (5% H_2 in Ar). The three diffraction peaks located at 2θ of 43.9°, 51.2°, and 75.3° are unambiguously assigned to the (111), (200), and (220) facets of a face-centered cubic (fcc) Cu–Ni alloy (JCPDS no.65–9047). No other diffraction peaks that would be suggestive of impurities were detected, such as metallic Cu (JCPDS no.70–3039) and Ni (JCPDS no.70–0989), indicating the formation of Cu–Ni solid solution during this process. The sharp diffraction peak is also indicative of

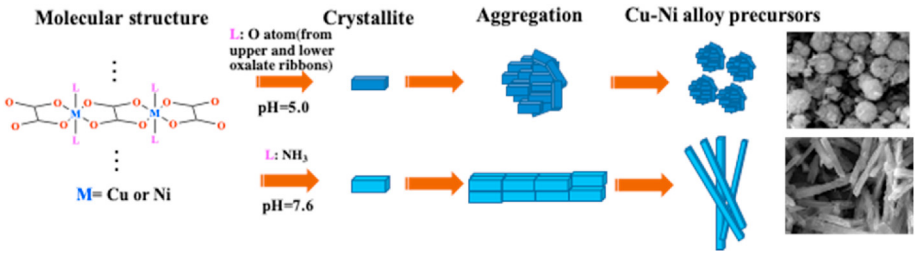

Fig. 5. NH_3-induced oriented-growth mechanism of rod-like Cu–Ni alloy precursor.

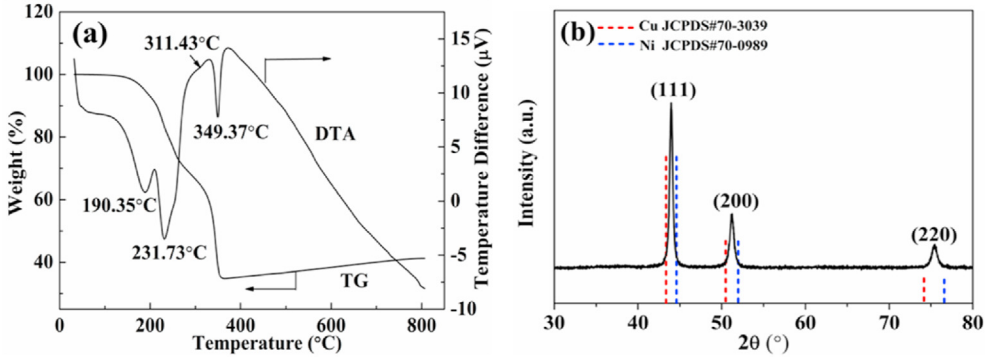

Fig. 6. (a) TG-DTA curves of the rod-like Cu–Ni alloy precursor (obtained at pH = 7.6) in the Ar atmosphere. (b) XRD pattern Cu–Ni alloy rods and Cu (red dash line) and Ni (blue dash line) references.

the high crystallinity of this material. The mean crystallite size of alloy particles was further calculated to be 20.7 nm through the Scherrer equation [48,49]: $D = k\lambda/B\cos\theta$, where k is Scherrer constant (taken as 0.89), other parameters including λ, B, θ represent the wavelength of X-ray source (0.154056 nm), full width at half the maximum intensity (FWHM) and the peak position, respectively.

Electron microscopy techniques were applied to observe the morphology and microstructure of the as-prepared Cu–Ni alloy particles. The SEM image shown in Fig. 7a indicates the Cu–Ni alloy perfectly inherits the quasi-one-dimensional morphology of the precursor obtained at pH = 7.6 with diameters of 0.4–0.6 μm and lengths of tens of micrometers. The porous structure we observe

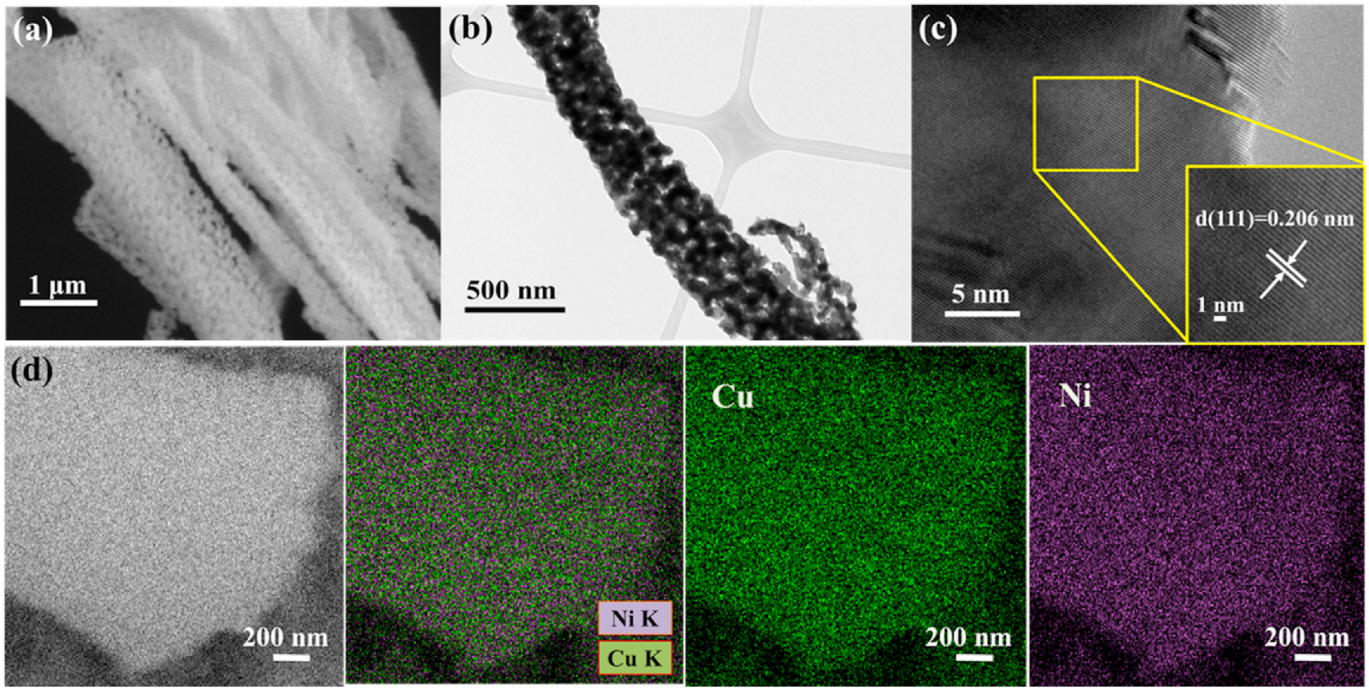

Fig. 7. (a) SEM, (b) TEM, (c) HRTEM images and (d) elemental mapping of Cu–Ni alloy rods.

likely results from the release of volatiles such as NH_3, H_2O, and CO_2 during the annealing process [50]. It can also be seen from the TEM image (Fig. 7b) that the rod is constructed by numerous interconnected nanoscale particles and nanopores, which could endow the Cu–Ni alloy with the prominently enlarged SSA. The HR-TEM image of Fig. 7c displays the distinct lattice fringes with an interplanar distance of 0.206 nm (inset image) and this can be indexed to the (111) crystal plane of the Cu–Ni alloy. EDX analysis results of two selected areas shown in Fig. S1 demonstrates that the atomic ratio for Cu and Ni is 1:1, and the elemental mapping result indicates their uniform distribution over Cu–Ni alloy rods (Fig. 7d). The elemental valence states of Cu–Ni alloy rods in the near-surface region were examined by XPS and the corresponding spectra and the deconvoluted peaks are displayed in Fig. S2. The survey spectrum (Fig. S2a) shows the appearance of the peaks of Cu, Ni, and O elements, implying the existence of oxidized states on the surface of alloy powders. The high-resolution XPS spectrum of Ni 2p (Fig. S2b) exhibits the fitted peaks corresponding to metallic Ni^0 at around 870.3 eV and 852.8 eV and Ni^{2+} located at 873.5 eV and 855.8 eV for Ni $2p_{1/2}$ and Ni $2p_{3/2}$, respectively [12]. Besides, the peaks with the binding energy of 879.5 eV and 861.4 eV are ascribed to shakeup satellites of Ni^{2+}. The presence of nickel oxides enables the potential promotion of the formation of the electroactive intermediates, which is conducive to facilitate the EOR process. Likewise, The XPS spectrum of Cu 2p (Fig. S2c) also shows the fitting peaks of metallic Cu^0 and Cu^{2+} at 952.4 eV and 954.7 eV for Cu $2p_{1/2}$ and 932.6 eV and 934.6 eV for Cu $2p_{3/2}$ [51], respectively, whereas the other peaks fitted in the spectrum are assigned to the satellites of Cu^0 (962.3 eV and 941.9 eV) and Cu^{2+} (962.8 eV and 944.0 eV). The partial oxidation of Ni and Cu in the surface region resulting from their exposure to the air could prevent the further oxidation of the inner metallic phase. Moreover, the surface atomic ratio of Cu and Ni obtained by XPS analysis was near 1:1, which is consistent with the above EDX results and the predetermined Cu–Ni ratio in the raw materials, further indicating the uniform distribution of Cu and Ni in the alloy rods.

To further elucidate and clarify their pore structure, the SSA and the pore size distribution of the as-prepared Cu–Ni alloy rods were measured through the N_2 adsorption/desorption technique. The isotherms are presented in Fig. 8, which displays a typical IV type Langmuir curve with a hysteresis loop, indicating the mesoporous structure of Cu–Ni alloy rods [52]. As displayed in the inset image of Fig. 8, the corresponding Barrett-Joyner-Halenda (BJH) pore size distribution shows a hierarchical distribution of pores where a relatively narrow peak and a broad peak are located at around 2.47 nm and 29.30 nm, respectively. The average pore diameter of

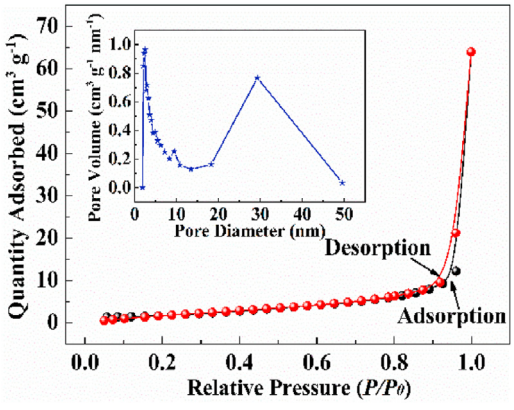

Fig. 8. N_2 adsorption and desorption isotherms for Cu–Ni alloy rods (inset image: pore size distribution).

Cu–Ni alloy rods was calculated to be 30.97 nm and the Brunauer-Emmett-Teller (BET) surface area is 6.84 $m^2\ g^{-1}$, which is close to that of the reported quasi-1D porous nickel powders (7.9 $m^2\ g^{-1}$) [33]. It is expected that the hierarchical mesoporous structure and the large SSA of the prepared Cu–Ni alloy rods could provide sufficient active sites and shorten the electronic transportation and ionic diffusion pathways, significantly improving electrocatalytic activity comparing with nonporous materials when being used on the interface of electrolyte and electrodes.

3.3. Electrocatalytic test for Cu–Ni alloy rods

Cyclic voltammetry (CV) tests of Cu–Ni/GCE in 1 M NaOH solution in the absence and presence of ethanol (scan rate: 20 mV s^{-1}) were both conducted to investigate the electrocatalytic property of Cu–Ni alloy rods for EOR at the room temperature. In Fig. 9a, when using blank NaOH as the electrolyte, a pair of the redox peaks at the potential around 0.35 V and 0.50 V (vs. SCE) is observed, which could be ascribed to the diffusion-controlled transformation between $Ni(OH)_2$ and NiOOH [12,48,53]. After the addition of 0.1 M ethanol in solution, due to the surface-active substance of Ni (III), ethanol molecules tend to be oxidized and a peak with the current density of ~50 mA cm^{-2} is observed at 0.65 V, which is about two times higher than that of porous Ni fibers (~22 mA cm^{-2} shown in Fig. S3). The following descending current response might be associated with the diminished reaction rate arising from the depletion of ethanol molecules near the surface of the electrode and their slow diffusion from the bulk solution. Owing to the refreshed surface of electrocatalyst by reactivation of Ni (III) from Ni (II) at high potentials, ethanol or intermediates absorbed can be still electro-oxidized [54,55], leading to the slower decrease of current density at 0.65–0.7 V during the reverse scan. Since the electrocatalytic reaction mainly takes place at the surface of active materials, only portions of NiOOH are consumed during the EOR process [48], making the cathodic peak still recognizable. However, unlike the decreased cathodic current density on Ni/GCE (Fig. S3), the slightly increased current density observed in Fig. 9a on Cu–Ni/GCE might be related to the continuous activation of electrocatalyst during the CV test, i.e., thicker layer of NiOOH was formed with the increased numbers of sweeping cycles [53].

Cyclic voltammograms of Cu–Ni/GCE in NaOH with various concentrations of ethanol are also recorded in Fig. 9b. From 0 M to 0.2 M, the onset potentials negatively shift with the increasing current density of the anodic peak during the forward scan. Impressively, the anodic peak current density reaches as high as 86.10 mA cm^{-2} when adding 0.2 M of ethanol in the electrolyte, which is competitive to most of those reported Ni-based EOR electrocatalysts listed in Table S1. It should be admitted that the onset potential for ethanol oxidation on Cu–Ni/GCE is not comparable to that of the commercial Pt/C (0.009 V vs. SCE) or Pd/C (0.159 V vs. SCE) [56]. However, the recently reported onset potential as low as −0.086 V (vs. SCE) on CuNiPt ternary alloy nanoparticles supported on graphite pencil lead electrode (GPLE) [57] in an acidic environment might give us the hint that this issue could probably be solved by integrating the prepared Cu–Ni alloy rods with Pt/Pd nanoparticles or fabricating the novel rod-like Pt/Pd-involved multi-component alloys.

The electrocatalytic mechanism of Ni-based alloy/composites has been well studied in the few past decades, which illustrated that the component of Ni in these materials mainly serves as the active substances for the oxidation of SOMs [30,58]. Similarly, the whole process for EOR on the fabricated Cu–Ni/GCE could be described as follows [12,13,59,60]:

$$Ni + 2OH^- \rightarrow Ni(OH)_2 + 2e^- \quad (1)$$

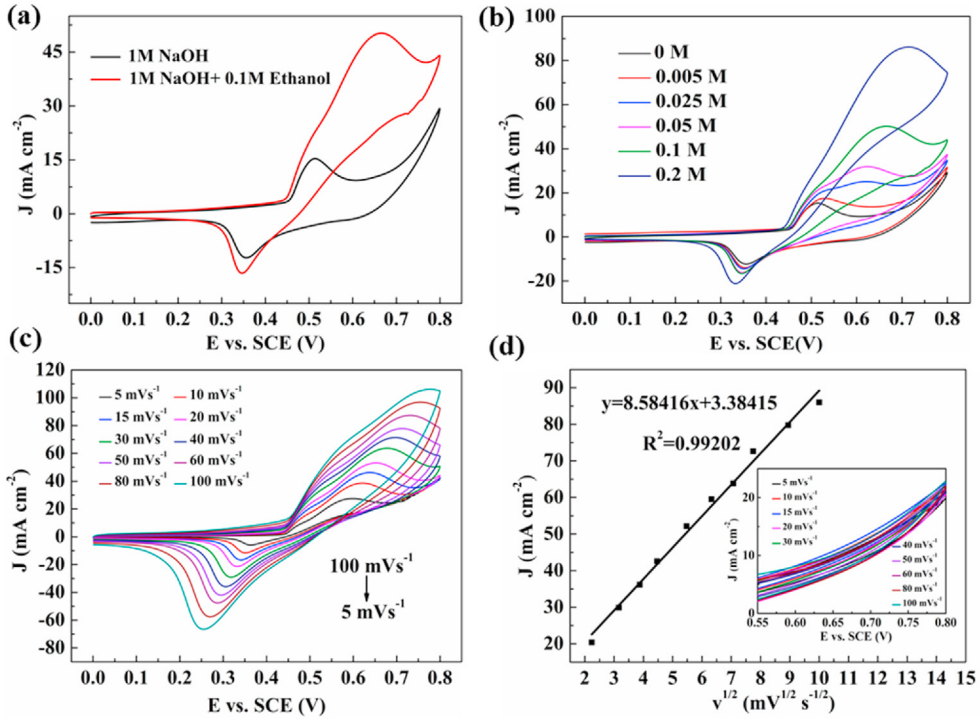

Fig. 9. Cyclic voltammograms of Cu–Ni/GCE (a) in 1 M NaOH solution in the presence and absence of 0.1 M ethanol (scan rate: 20 mV s^{-1}); (b) in 1 M NaOH solution containing various concentrations of ethanol (scan rate: 20 mV s^{-1}); (c) in 1 M NaOH solution with 0.1 M ethanol at different scan rates (5 mV s^{-1}–100 m V s^{-1}); and (d) relationship between the anodic current densities and the square root of the scan rates; inset image: background current densities of Cu–Ni/GCE measured in 1 M NaOH solution at the scan rates from 5 mV s^{-1} to 100 mV s^{-1}.

$$Ni(OH)_2 + OH^- \rightleftharpoons NiOOH + H_2O + e^- \quad (2)$$

$$NiOOH + \text{ethanol} \rightarrow Ni(OH)_2 + \text{products} \quad (3)$$

After immersing the modified electrode in the alkaline media, $Ni(OH)_2$ thin layer immediately forms on the surface of the electrocatalyst (Eq. (1)) and is then oxidized to NiOOH during the forward sweeping, corresponding to the current peak at 0.5 V in the blank NaOH solution (Eq. (2)) [48]. With the addition of ethanol in the electrolyte, the ethanol will be oxidized to intermediates or final products, i.e., acetaldehyde or acetic acid, parallel to the reduction of NiOOH to $Ni(OH)_2$ (Eq. (3)). The repeat of processes described in Eq. (2) and Eq. (3) leads to the continuous electrooxidation of ethanol molecules on the electrode. Cu atoms are thought to contribute significantly to finely tune the electronic structure of Ni and preventing the transformation of NiOOH from β-phase to γ-phase, where the latter one is a passivating electrochemical species and usually shows the inferior activity to β-NiOOH in alkaline media [12,61].

The CVs of Cu–Ni/GCE measured at different scan rates ranging from 5 mV s^{-1} to 100 mV s^{-1} in the presence of 0.1 M ethanol were plotted in Fig. 9c. Faster potential scans could usually decrease the thickness of the diffusion layer, leading to the higher obtained current densities of anodic peaks relating to ethanol oxidation on the electrode surface [62]. Besides, the corresponding potentials are observed shifting positively when increasing the scan rates. The anodic peak current densities subtracting the background current (measured without ethanol) are plotted with a linear response against the square root of scan rates (Fig. 9d), which implies that the electrocatalytic oxidation reaction of ethanol on the Cu–Ni/GCE might be a diffusion-controlled process that is consistent with the previous reports [10,39,63]. Tafel plots derived from linear sweep voltammetry (LSV) measured at the scan rate of 1 mV s^{-1} with 0.1 M ethanol are displayed in Fig. S4, where the Cu–Ni/GCE and Ni/GCE demonstrate the slopes of 236 mV dec^{-1} and 352 mV dec^{-1}, respectively, indicating the faster charge transfer and more active electro-oxidation of ethanol molecules on Cu–Ni/GCE than Ni/GCE.

In order to evaluate the electrocatalytic stability of the Cu–Ni alloy rods, chronoamperometry (CA) testing was performed in an electrolyte of 1 M NaOH solution with 0.1 M ethanol at the polarization potential of 0.6 V (vs. SCE) for 2000 s, as displayed in Fig. 10. The current density decreased rapidly due to the double-layer charging and the adsorption of intermediates on the active sites of electrocatalyst [39]. After that, it gradually reached a quasi-equilibrium steady-state and maintained 95% of the original current density measured at 100 s after 2000 s, indicating their good

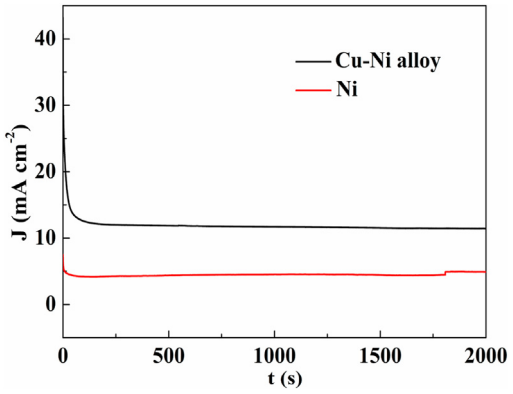

Fig. 10. CA curve of Cu–Ni/GCE and Ni/GCE at 0.6 V (vs. SCE) for 2000 s (electrolyte: 1 M NaOH solution in the presence of 0.1 M ethanol).

long-term stability. Moreover, the steady current of Cu–Ni/GCE during the whole process is observed constantly higher than that of Ni/GCE with the same mass loading and test conditions as shown in Fig. 10, which further confirms the relative superior electrocatalytic performance of Cu–Ni alloy rods for the EOR process.

4. Conclusions

In summary, highly dispersed Cu–Ni alloy particles with a rod-like morphology and hierarchical porous structure were successfully prepared via a simple template-free approach, combining a coordination-precipitation process and the post thermal treatment. To achieve the compositional homogeneity and uniform distribution of Cu and Ni in alloy products, water-ethanol mixture as the solvent was used to prepare Cu–Ni alloy precursors. The addition of NH_3 not only adjusted the pH of the solution, but also shaped the Cu–Ni alloy precursors into the quasi-one-dimensional morphology when a pH of 7.6 was maintained, and the corresponding NH_3-induced oriented growth mechanism was proposed. After thermal decomposition, well-alloyed Cu–Ni rods were obtained in good crystallinity, with a high BET surface area of 6.84 $m^2 g^{-1}$, an average pore diameter of 30.97 nm, and the desired atomic ratio of Cu/Ni = 1:1. A large anodic current density of 86.10 mA cm^{-2} in presence of 0.2 M ethanol and retention of 95% original current density after 2000 s indicated the excellent electrocatalytic activity of this material, and its high stability for the EOR in alkaline media. This work may offer a promising strategy for large-scale synthesis of Ni-based alloys or compounds that could serve as high-performance anodic electrocatalysts for DEFCs.

CRediT authorship contribution statement

Zelin Miao: Investigation, Writing - original draft. **Changfan Xu:** Investigation, Writing - review & editing. **Jing Zhan:** Supervision, Conceptualization, Writing - review & editing, Funding acquisition. **Ziwei Xu:** Validation.

Declaration of competing interest

The authors declare that they have no known competing financial interests or personal relationships that could have appeared to influence the work reported in this paper.

Acknowledgments

This work was financially supported by the Natural Science Foundation of Hunan Province, China (2020JJ4735); Science and Technology Department of Hunan Province Tackling Key Scientific and Technological Problems and Transformation of Major Scientific and Technological Achievements (2018GK4001); and the Hunan Key Laboratory for Rare Earth Functional Materials (2017TP1031). The authors acknowledge Dr. Michael S. Inkpen and Mr. Joseph M. Parr in the Department of Chemistry, University of Southern California for their insightful suggestions and language modification.

Appendix A. Supplementary data

Supplementary data to this article can be found online at https://doi.org/10.1016/j.jallcom.2020.157438.

References

[1] A.E. Fetohi, R.S. Amin, R.M.A. Hameed, K.M. El-Khatib, Effect of nickel loading in Ni@Pt/C electrocatalysts on their activity for ethanol oxidation in alkaline medium, Electrochim. Acta 242 (2017) 187–201, https://doi.org/10.1016/j.electacta.2017.05.022.
[2] Y. Qin, Z. Xiong, J. Ma, L. Yang, Z. Wu, W. Feng, T. Wang, W. Wang, C. Wang, Enhanced electrocatalytic activity and stability of Pd nanoparticles supported on TiO_2-modified nitrogen-doped carbon for ethanol oxidation in alkaline media, Int. J. Hydrogen Energy 42 (2017) 1103–1112, https://doi.org/10.1016/j.ijhydene.2016.09.060.
[3] W. Huang, X. Ma, H. Wang, R. Feng, J. Zhou, P.N. Duchesne, P. Zhang, F. Chen, N. Han, F. Zhao, J. Zhou, W. Cai, Y. Li, Promoting effect of $Ni(OH)_2$ on palladium nanocrystals leads to greatly improved operation durability for electrocatalytic ethanol oxidation in alkaline solution, Adv. Mater. 29 (2017) 1703057, https://doi.org/10.1002/adma.201703057.
[4] Z. Li, Y. Chen, G. Fu, Y. Chen, D. Sun, J. Lee, Y. Tang, Porous PdRh nanobowls: facile synthesis and activity for alkaline ethanol oxidation, Nanoscale 11 (2019) 2974–2980, https://doi.org/10.1039/C8NR09482A.
[5] S. Sarkar, R. Jana, H. Vadlamani, S. Ramani, D. Mumbaraddi, S.C. Peter, Facile aqueous-phase synthesis of the PtAu/Bi_2O_3 hybrid catalyst for efficient electro-oxidation of ethanol, ACS Appl. Mater. Interfaces 9 (2017) 15373–15382, https://doi.org/10.1021/acsami.7b00083.
[6] K.M. El-Khatib, R.M. Abdel Hameed, R.S. Amin, A.E. Fetohi, Core-shell structured Cu@Pt nanoparticles as effective electrocatalyst for ethanol oxidation in alkaline medium, Int. J. Hydrogen Energy 42 (2017) 14680–14696, https://doi.org/10.1016/j.ijhydene.2017.04.118.
[7] A. Dutta, A. Mondal, J. Datta, Tuning of platinum nano-particles by Au usage in their binary alloy for direct ethanol fuel cell: controlled synthesis, electrode kinetics and mechanistic interpretation, J. Power Sources 283 (2015) 104–114, https://doi.org/10.1016/j.jpowsour.2015.01.113.
[8] K. Kakaei, A. Rahimi, S. Husseindoost, M. Hamidi, H. Javan, A. Balavandi, Fabrication of Pt-CeO_2 nanoparticles supported sulfonated reduced graphene oxide as an efficient electrocatalyst for ethanol oxidation, Int. J. Hydrogen Energy 41 (2016) 3861–3869, https://doi.org/10.1016/j.ijhydene.2016.01.013.
[9] Y. Feng, D. Bin, B. Yan, Y. Du, T. Majima, W. Zhou, Porous bimetallic PdNi catalyst with high electrocatalytic activity for ethanol electrooxidation, J. Colloid Interface Sci. 493 (2017) 190–197, https://doi.org/10.1016/j.jcis.2017.01.035.
[10] J. Zhan, M. Cai, C. Zhang, C. Wang, Synthesis of mesoporous $NiCo_2O_4$ fibers and their electrocatalytic activity on direct oxidation of ethanol in alkaline media, Electrochim. Acta 154 (2015) 70–76, https://doi.org/10.1016/j.electacta.2014.12.078.
[11] Y. Wang, S. Zou, W. Cai, Recent advances on electro-oxidation of ethanol on Pt- and Pd-based catalysts: from reaction mechanisms to catalytic materials, Catalysts 5 (2015) 1507–1534, https://doi.org/10.3390/catal5031507.
[12] Y. An, H. Ijaz, M. Huang, J. Qu, S. Hu, The one-pot synthesis of CuNi nanoparticles with a Ni-rich surface for the electrocatalytic methanol oxidation reaction, Dalton Trans. 49 (2020) 1646–1651, https://doi.org/10.1039/C9DT04661E.
[13] I. Danaee, M. Jafarian, F. Forouzandeh, F. Gobal, M.G. Mahjani, Electrocatalytic oxidation of methanol on Ni and NiCu alloy modified glassy carbon electrode, Int. J. Hydrogen Energy 33 (2008) 4367–4376, https://doi.org/10.1016/j.ijhydene.2008.05.075.
[14] Y. Shen, A.C. Lua, Polyol synthesis of nickel-copper based catalysts for hydrogen production by methane decomposition, Int. J. Hydrogen Energy 40 (2015) 311–321, https://doi.org/10.1016/j.ijhydene.2014.10.071.
[15] Y. Shen, Y. Zhou, D. Wang, X. Wu, J. Li, J. Xi, Nickel-copper alloy encapsulated in graphitic carbon shells as electrocatalysts for hydrogen evolution reaction, Adv. Energy Mater. 8 (2018) 1701759, https://doi.org/10.1002/aenm.201701759.
[16] R. Solmaz, A. Döner, G. Kardas, Electrochemical deposition and characterization of NiCu coatings as cathode materials for hydrogen evolution reaction, Electrochem. Commun. 10 (2008) 1909–1911, https://doi.org/10.1016/j.elecom.2008.10.011.
[17] R. Ding, J. Liu, J. Jiang, F. Wu, J. Zhu, X. Huang, Tailored Ni–Cu alloy hierarchical porous nanowire as a potential efficient catalyst for DMFCs, Catal. Sci. Technol. 1 (2011) 1406–1411, https://doi.org/10.1039/C1CY00164G.
[18] I.S. Pieta, A. Rathi, P. Pieta, R. Nowakowski, M. Hołdynski, M. Pisarek, A. Kaminska, M.B. Gawande, R. Zboril, Electrocatalytic methanol oxidation over Cu, Ni and bimetallic Cu-Ni nanoparticles supported on graphitic carbon nitride, Appl. Catal., B 244 (2019) 272–283, https://doi.org/10.1016/j.apcatb.2018.10.072.
[19] B. Habibi, N. Delnavaz, Electrooxidation of glycerol on nickel and nickel alloy (Ni-Cu and Ni-Co) nanoparticles in alkaline media, RSC Adv. 6 (2016) 31797–31806, https://doi.org/10.1039/C5RA26006J.
[20] D. Huo, M.J. Kim, Z. Lyu, Y. Shi, B.J. Wiley, Y. Xia, One-dimensional metal nanostructures: from colloidal syntheses to applications, Chem. Rev. 119 (2019) 8972–9073, https://doi.org/10.1021/acs.chemrev.8b00745.
[21] T.W. Hansen, A.T. Delariva, S.R. Challa, A.K. Datye, Sintering of catalytic nanoparticles: particle migration or Ostwald ripening? Acc. Chem. Res. 46 (2013) 1720–1730, https://doi.org/10.1021/ar3002427.
[22] J. Chen, G. Zou, W. Deng, Z. Huang, X. Gao, C. Liu, S. Yin, H. Liu, X. Deng, Y. Tian, J. Li, C. Wang, D. Wang, H. Wu, L. Yang, H. Hou, X. Ji, Pseudo-bonding and electric-field harmony for Li-rich Mn-based oxide cathode, Adv. Funct. Mater. (2020) 2004302, https://doi.org/10.1002/adfm.202004302.
[23] J. Zhan, Z. Miao, M. Cai, Q. Li, Boosting ethanol oxidation over nickel oxide through construction of quasi-one-dimensional morphology and hierarchically porous structure, Trans. Nonferrous Metals Soc. China 30 (2020) 1615–1624, https://doi.org/10.1016/S1003-6326(20)65324-9.

[24] R. Chen, H. Wang, J. Miao, H. Yang, B. Liu, A flexible high-performance oxygen evolution electrode with three-dimensional $NiCo_2O_4$ core-shell nanowires, Nano Energy 11 (2015) 333–340, https://doi.org/10.1016/j.nanoen.2014.11.021.
[25] Y. Su, Q. Xu, G. Chen, H. Cheng, N. Li, Z. Liu, One dimensionally spinel $NiCo_2O_4$ nanowire arrays: facile synthesis, water oxidation, and magnetic properties, Electrochim. Acta 174 (2015) 1216–1224, https://doi.org/10.1016/j.electacta.2015.06.092.
[26] S. Alleg, S. Souilah, K. Dadda, J.J. Suñol, E.K. Hlil, H. Lassri, Investigation of the critical behavior and magnetocaloric properties in the nanocrystalline CuNi powders, J. Magn. Magn Mater. 444 (2017) 54–60, https://doi.org/10.1016/j.jmmm.2017.08.010.
[27] M. Gao, C. Yang, Q. Zhang, Y. Yu, Y. Hua, Y. Li, P. Dong, Electrochemical fabrication of porous Ni-Cu alloy nanosheets with high catalytic activity for hydrogen evolution, Electrochim. Acta 215 (2016) 609–616, https://doi.org/10.1016/j.electacta.2016.08.145.
[28] Z. Lin, J. Li, L. Li, L. Yu, W. Li, G. Yang, Manipulating the hydrogen evolution pathway on composition-tunable CuNi nanoalloys, J. Mater. Chem. 5 (2017) 773–781, https://doi.org/10.1039/C6TA09169E.
[29] R.O. Apaydin, B. Ebin, S. Gürmen, Single-step production of nanostructured copper-nickel (CuNi) and copper-nickel-indium (CuNiIn) alloy particles, Metall. Mater. Trans. 47 (2016) 3744–3752, https://doi.org/10.1007/s11661-016-3514-7.
[30] X. Tian, X. Zhao, L. Zhang, C. Yang, Z. Pi, S. Zhang, Performance of ethanol electro-oxidation on Ni-Cu alloy nanowires through composition modulation, Nanotechnology 19 (2008) 215711, https://doi.org/10.1088/0957-4484/19/21/215711.
[31] J.A. Dean, Lange's Handbook of Chemistry, fourteenth ed., McGraw-Hill, Inc., New York; London, 1999.
[32] J. Wu, G. Liu, T. Su, W. Zhang, M. Luo, T. Wei, Preparation of fibrous nickel powder by precipitation transformation coupled with thermal decomposition, Trans. Nonferrous Metals Soc. China 25 (2015) 2653–2660, https://doi.org/10.1016/S1003-6326(15)63888-2.
[33] Y. Long, J. Zhan, J. Huang, Porous nickel fibers with enhanced electrocatalytic activities on electro-oxidation of ethanol in alkaline media, JOM 71 (2019) 1485–1491, https://doi.org/10.1007/s11837-019-03363-5.
[34] J. Zhan, Y. He, D. Zhou, C. Zhang, Thermodynamic analysis on synthesis of fibrous Ni-Co alloys precursor and Ni/Co control, Trans. Nonferrous Metals Soc. China 21 (2011) 1141–1148, https://doi.org/10.1016/S1003-6326(11)60834-0.
[35] Y. Fan, C. Zhang, J. Zhan, J. Wu, Thermodynamic equilibrium calculation on preparation of copper oxalate precursor powder, Trans. Nonferrous Metals Soc. China 18 (2008) 454–458, https://doi.org/10.1016/S1003-6326(08)60080-1.
[36] Y. Yao, C. Zhang, J. Zhan, F. Ding, J. Wu, Thermodynamics analysis of Ni^{2+}-$C_2H_8N_2$-$C_2O_4^{2-}$-H_2O system and preparation of Ni microfiber, Trans. Nonferrous Metals Soc. China 23 (2013) 3456–3461, https://doi.org/10.1016/S1003-6326(13)62888-5.
[37] Y. Lv, X. Wu, D. Wu, D. Huo, S. Zhao, Synthesis of barium fluoride nanoparticles by precipitation in ethanol-aqueous mixed solvents, Powder Technol. 173 (2007) 174–178, https://doi.org/10.1016/j.powtec.2006.12.018.
[38] Y. Jiang, S. Xu, Z. Zhao, L. Zheng, Z. Wang, C. Wang, Y. Cui, Water-ethanol solvent mixtures: a promising liquid environment for high quality positively-charged CdTe nanocrystal preparation, RSC Adv. 5 (2015) 18379–18383, https://doi.org/10.1039/C4RA14134B.
[39] G.M. Tomboc, M.W. Abebe, A.F. Baye, H. Kim, Utilization of the superior properties of highly mesoporous PVP modified $NiCo_2O_4$ with accessible 3D nanostructure and flower-like morphology towards electrochemical methanol oxidation reaction, J. Energy Chem. 29 (2019) 136–146, https://doi.org/10.1016/j.jechem.2018.08.009.
[40] Y. Yang, G. Huang, H. Sun, M. Ahmad, Q. Mou, H. Zhang, Preparation and electrochemical properties of mesoporous $NiCo_2O_4$ double-hemisphere used as anode for lithium-ion battery, J. Colloid Interface Sci. 529 (2018) 357–365, https://doi.org/10.1016/j.jcis.2018.06.039.
[41] J. Zhan, D. Zhou, C. Zhang, Shape-controlled synthesis of novel precursor for fibrous Ni-Co alloy powders, Trans. Nonferrous Metals Soc. China 21 (2011) 544–551, https://doi.org/10.1016/S1003-6326(11)60749-8.
[42] Y. Fan, C. Zhang, J. Wu, J. Zhan, P. Wang, Composition and morphology of complicated copper oxalate powder, Trans. Nonferrous Metals Soc. China 20 (2010) 165–170, https://doi.org/10.1016/S1003-6326(09)60115-1.
[43] J. Chen, J. Zhan, Q. Li, Exploration and crystal phase engineering from bismuthinite ore to visible-light responsive photocatalyst of Bi_2O_3, J. Environ. Chem. Eng. 7 (2019) 103375, https://doi.org/10.1016/j.jece.2019.103375.
[44] M. Rohdenburg, P. Martinovic, K. Ahlenhoff, S. Koch, D. Emmrich, A. Gölzhaüser, P. Swiderek, Cisplatin as a potential platinum focused electron beam induced deposition precursor: NH_3 ligands enhance the electron-induced removal of chlorine, J. Phys. Chem. C 123 (2019) 21774–21787, https://doi.org/10.1021/acs.jpcc.9b05756.
[45] N. Jongen, P. Bowen, J. Lemaître, J. Valmalette, H. Hofmann, Precipitation of self-organized copper oxalate polycrystalline particles in the presence of hydroxypropylmethylcellulose (HPMC): control of morphology, J. Colloid Interface Sci. 226 (2000) 189–198, https://doi.org/10.1006/jcis.2000.6747.
[46] C. Zhang, Y. Yao, J. Zhan, J. Wu, C. Li, Template-free synthesis of Ni microfibres and their electromagnetic wave absorbing properties, J. Phys. D Appl. Phys. 46 (2013) 495308, https://doi.org/10.1088/0022-3727/46/49/495308.
[47] A.N. Christensen, B. Lebech, N.H. Andersen, J. Grivel, The crystal structure of paramagnetic copper (II) oxalate (CuC_2O_4): formation and thermal decomposition of randomly stacked anisotropic nano-sized crystallites, Dalton Trans. 43 (2014) 16754–16768, https://doi.org/10.1039/C4DT01689K.
[48] N. Spinner, W.E. Mustain, Effect of nickel oxide synthesis conditions on its physical properties and electrocatalytic oxidation of methanol, Electrochim. Acta 56 (2011) 5656–5666, https://doi.org/10.1016/j.electacta.2011.04.023.
[49] S.S. Jayaseelan, T. Ko, S. Radhakrishnan, C. Yang, H. Kim, B. Kim, Novel MWCNT interconnected $NiCo_2O_4$ aerogels prepared by a supercritical CO_2 drying method for ethanol electrooxidation in alkaline media, Int. J. Hydrogen Energy 41 (2016) 13504–13512, https://doi.org/10.1016/j.ijhydene.2016.05.175.
[50] X. Fang, J. Chen, J. Zhan, Heterojunction photocatalyst for organic degradation: superior photocatalytic activity through the phase and interphase engineering, Ceram. Int. 46 (2020) 23245–23256, https://doi.org/10.1016/j.ceramint.2020.05.317.
[51] H. Yen, Y. Seo, S. Kaliaguine, F. Kleitz, Role of metal-support interactions, particles size, and metal-metal synergy in CuNi nanoparticles for H_2 generation, ASC Catal. 5 (2015) 5505–5511, https://doi.org/10.1021/acscatal.5b00869.
[52] M. Yu, J. Chen, J. Liu, S. Li, Y. Ma, J. Zhang, J. An, Mesoporous $NiCo_2O_4$ nanoneedles grown on 3D graphene-nickel foam for supercapacitor and methanol electro-oxidation, Electrochim. Acta 151 (2015) 99–108, https://doi.org/10.1016/j.electacta.2014.10.156.
[53] N.A.M. Barakat, M. Motlak, A.A. Elzatahry, K.A. Khalil, E.A.M. Abdelghani, Ni_xCo_{1-x} alloy nanoparticle-doped carbon nanofibers as effective non-precious catalysts for ethanol oxidation, Int. J. Hydrogen Energy 39 (2014) 305–316, https://doi.org/10.1016/j.ijhydene.2013.10.061.
[54] A.B. Soliman, H.S. Abdel-Samad, S.S.A. Rehim, M.A. Ahmed, H.H. Hassan, High performance nano-Ni/Graphite electrode for electro-oxidation in direct alkaline ethanol fuel cells, J. Power Sources 325 (2016) 653–663, https://doi.org/10.1016/j.jpowsour.2016.06.088.
[55] Z. Wang, Y. Du, F. Zhang, Z. Zheng, Y. Zhang, C. Wang, High electrocatalytic activity of non-noble Ni-Co/graphene catalyst for direct ethanol fuel cells, J. Solid State Electrochem. 17 (2013) 99–107, https://doi.org/10.1007/s10008-012-1855-8.
[56] L. Ma, D. Chu, R. Chen, Comparison of ethanol electro-oxidation on Pt/C and Pd/C catalysts in alkaline media, Int. J. Hydrogen Energy 37 (2012) 11185–11194, https://doi.org/10.1016/j.ijhydene.2012.04.132.
[57] H. Imanzadeh, B. Habibi, Electrodeposition of ternary CuNiPt alloy nanoparticles on graphenized pencil lead electrode as a new electrocatalyst for electro-oxidation of ethanol, Solid State Sci. 105 (2020) 106239, https://doi.org/10.1016/j.solidstatesciences.2020.106239.
[58] V. Hassanzadeh, M.A. Sheikh-Mohseni, B. Habibi, Catalytic oxidation of ethanol by a nanostructured Ni-Co/RGO composite: electrochemical construction and investigation, J. Electroanal. Chem. 847 (2019) 113200, https://doi.org/10.1016/j.jelechem.2019.113200.
[59] M. Fleischmann, K. Korinek, D. Pletcher, The oxidation of organic compounds at a nickel anode in alkaline solution, J. Electroanal. Chem. 31 (1971) 39–49, https://doi.org/10.1016/S0022-0728(71)80040-2.
[60] M. Jafarian, R.B. Moghaddam, M.G. Mahjani, F. Gobal, Electro-catalytic oxidation of methanol on a Ni-Cu alloy in alkaline medium, J. Appl. Electrochem. 36 (2006) 913–918, https://doi.org/10.1007/s10800-006-9155-6.
[61] G.S. Theres, G. Velayutham, P.S. Krishnan, K. Shanthi, Synergistic impact of Ni-Cu hybrid oxides deposited on ordered mesoporous carbon scaffolds as non-noble catalyst for methanol oxidation, J. Mater. Sci. 54 (2019) 1502–1519, https://doi.org/10.1007/s10853-018-2884-1.
[62] N. Elgrishi, K.J. Rountree, B.D. McCarthy, E.S. Rountree, T.T. Eisenhart, J.L. Dempsey, A practical beginner's guide to cyclic voltammetry, J Chem. Educ. 95 (2018) 197–206, https://doi.org/10.1021/acs.jchemed.7b00361.
[63] M. Farsadrooh, M. Noroozifar, A.R. Modarresi-Alam, H. Saravani, Sonochemical synthesis of high-performance Pd@CuNWs/MWCNTs-CH electrocatalyst by galvanic replacement toward ethanol oxidation in alkaline media, Ultrason. Sonochem. 51 (2019) 478–486, https://doi.org/10.1016/j.ultsonch.2018.06.011.